Electrochimica Acta 211 (2016) 962–971

Contents lists available at ScienceDirect

Electrochimica Acta

journal homepage: www.elsevier.com/locate/electacta

MgO-template-assisted synthesis of worm-like carbon@MoS_2 composite for lithium ion battery anodes

Liu Wan[a], Wei Sun[a,c], Juanjuan Shen[a,b], Xiaocheng Li[a,*]

[a] Laboratory of Clean Energy Chemistry and Materials, Lanzhou Institute of Chemical Physics, Chinese Academy of Sciences, Lanzhou 730000, PR China
[b] Graduate University of Chinese Academy of Sciences, Beijing 100049, PR China
[c] School of Petrochemical Engineering, Lanzhou University of Technology, Lanzhou 730050, PR China

ARTICLE INFO

Article history:
Received 7 May 2016
Received in revised form 14 June 2016
Accepted 22 June 2016
Available online 23 June 2016

Keywords:
template-assisted synthesis
molybdenum disulfide
amorphous carbon
lithium-ion batteries

ABSTRACT

In this study, a facile MgO template-assisted route has been proposed for the preparation of carbon@MoS_2 composites via a one-step hydrothermal method followed by a thermal annealing process. By using sucrose as a carbon source and commercial MgO powder as a structure-directing agent, a three-dimensional sphere-like carbon@MoS_2 nanoarchitecture was assembled by one-dimensional worm-like nanorods which were composed of few-layered MoS_2 nanosheets and amorphous carbon matrix. The influence of different amount of MgO template on the morphology, structure, and lithium storage performance of the carbon@MoS_2 composites is systematically investigated. The carbon@MoS_2-2 composite synthesized with a Mo precursor: MgO molar ratio of 1:1 exhibits much higher reversible capacity (905.3 mAh g^{-1} after 100 cycles at a current density of 100 mA g^{-1}) and better high-rate capability (503.4 mAh g^{-1} at 5000 mA g^{-1}) than those of bare MoS_2 and template-free carbon@MoS_2-0 composite. Impressively, superior cycling stability is achieved for the carbon@MoS_2-2 composite with a capacity retention of 93.4% even after 400 charge/discharge cycles at 5000 mA g^{-1}. The excellent electrochemical performance for carbon@MoS_2-2 composite can be ascribed to its unique hierarchical nanoarchitecture and synergetic effect between MoS_2 nanosheets and amorphous carbon.

1. Introduction

In recent years, lithium ion batteries (LIBs) have attracted extensive attention and become the main power sources for electric devices and grid energy storage systems [1–4]. However, traditional anode electrode materials such as commercial graphite cannot fulfill the increasing demand for high energy density and power density, due to its low theoretical specific capacity (372 mAh g^{-1}) and poor rate-capability [5,6]. Therefore, alternative anode materials with large specific capacities, high rate performance, and long-cycle properties are desirable for high-performance LIBs.

Molybdenum disulfide (MoS_2), a typical layered transition metal sulfide, is comprised of covalently bonded three stacked atom layers (S-Mo-S) held together by weak van der Waals interaction [7,8]. Owing to its unique chemical peculiarities and high capacity (~670 mAh g^{-1}), MoS_2-based nanostructured materials have been demonstrated to be the ideal anode materials for LIBs [9,10]. However, most MoS_2-based electrodes still suffer from the low electronic/ionic conductivity, rapid capacity fading as well as poor cycling stability [9,11,12]. To address these issues, one feasible strategy is to construct the MoS_2/carbon composites through introducing conductive carbonaceous materials (such as graphene [13], carbon nanotubes [14], and amorphous carbon [15]). These conducting agent in carbon/MoS_2 composites can serve as a good conductive network and a buffering layer to accommodate substantial volume change of MoS_2 during repeated lithiation/delithiation process, thereby leading to improved rate and cycling performances [13–15]. Another strategy is to design various morphologies of nanostructured MoS_2 (such as nanosheets [16], nanotubes [17], nanoplates [18], nanoboxes [19], nanocables [20], and microspheres [21]). Owing to their large surface area, short diffusion path, and abundant active sites for lithium storage, nanostructured MoS_2 electrodes delivered greatly enhanced electrochemical properties of LIBs with higher reversible capacities and prolonged lifespan [22].

To fabricate nanostructured MoS_2-based hybrids, various metal oxides with unique morphologies (such as Fe_2O_3 nanocubes [19], TiO_2 nanotubes [23], TiO_2 nanospheres [24], and SiO_2 nanospheres [25]) have been utilized as the hard templates. These templates

* Corresponding author. Tel.: +86 931 4968040; fax: +86 931 4968040.
E-mail addresses: xiaocheng@licp.cas.cn, lixch2001@126.com (X. Li).

http://dx.doi.org/10.1016/j.electacta.2016.06.115
0013-4686/

usually act as the supporting matrix and the core of the hybrid nanoarchitectures to grow MoS_2, which plays a key role in the formation of the MoS_2-based hybrids with rational nanoscale structure [1,19]. However, the drawbacks of the hard template method are the complicated, time-consuming steps to synthesize the solid scaffolds by complex techniques. Compared with the above mentioned templates, commercial magnesium oxide powder exhibits the following advantages: (1) natural abundance and low cost; (2) the preparation of MoS_2 and magnesium hydroxide nanoplate template (converted from commercial MgO powder) can be achieved in one step via one-pot hydrothermal technique in the absence of any surfactants [15,26], which reduces the preparation steps and saves time; (3) the template can be easily removed by HCl solution at room temperature. In addition, MoS_2 nanocomposites obtained via a MgO template method have not been reported on its application as high-performance LIBs anodes.

In the present work, we present a simple and facile process to synthesize carbon@MoS_2 composite via one-pot hydrothermal method with the aid of commercial MgO powder followed by annealing in H_2/N_2 atmosphere at 750 °C. With the synergistic effects from sucrose as a binder and the MgO template as a structure-directing agent, a three-dimensional (3D) sphere-like carbon@MoS_2 composite is constructed by loosely stacked, worm-like one-dimensional (1D) nanorods, which are homogeneously coated with amorphous carbon. When evaluated as anode materials for LIBs, the carbon@MoS_2 composite shows a high reversible capacity, high-rate capability and excellent cycling performance.

2. Experimental

2.1. Synthesis of C@MoS_2 composite

In a typical experiment, certain amounts of the commercial MgO powders were dispersed into 20 mL of deionized water and followed by ultrasonication for 1 h. After that, Na_2MoO_4 (0.15 g), NH_2CSNH_2 (0.4 g), and sucrose (0.25 g) were dissolved in 15 mL of deionized water and sonicated for 15 min. Then, the resulting mixed solution was dropped into the MgO suspension under stirring followed by sonication for 1 h. Subsequently, the resulting solution was transferred into a 50 mL Teflon-lined stainless steel autoclave and heated at 180 °C for 24 h. After cooling naturally, the precipitates were filtered and washed several times with deionized water and ethanol, followed by drying at 80 °C for 12 h. Then, the powder was calcined at 750 °C for 2 h under H_2/Ar (5: 95 v/v) atmosphere with a ramp rate of 5 °C min^{-1}. Finally, the C@MoS_2 composites were collected by etching with hydrochloric acid solution (4.0 M) for 12 h, followed by washing with water and ethanol for several times. Surface morphology and structure of the C@MoS_2 composites were tailored by adjusting the amount of MgO powder (0.0, 12.5. 25.0, and 50.0 mg) during synthesis process, and the resulting products were named as C@MoS_2-0, C@MoS_2-1, C@MoS_2-2, and C@MoS_2-3, respectively. For comparison, bare MoS_2 was also synthesized by the same procedure without adding sucrose and MgO powder. The sucrose-derived amorphous carbon was obtained in the absence of Na_2MoO_4, NH_2CSNH_2 and MgO powder.

2.2. Characterization

The morphology of the as-prepared samples were characterized by a field-emission electron microscope (FESEM; JSM-6701, JOEL) and a high-resolution transmission electron microscope (HRTEM; JEM 2010F, JOEL) operated at 200 kV. The crystal structures were investigated by a X-ray diffractometer (XRD, D/max-2400, Digaku, Japan) with a radiation from a Cu target (Kα, λ = 0.1541 nm). Raman spectrum was recorded on a Jobin Yvon Labor Raman HR-800 spectrometer with a 514 nm Ar ion laser as excitation source. Thermogravimetric analysis (TGA) was recorded from room temperature to 800 °C in air with a ramp rate of 10 °C min^{-1}. N_2 adsorption isotherms were measured using a Micromeritics ASAP2020 analyzer at 77 K. Before measurements, all samples were degassed at 473 K for 12 h. The Brunauer–Emmett–Teller (BET) method was utilized to calculate the specific gravimetric surface areas (S_{BET}). The total pore volume values (V_{total}) were estimated from the adsorbed amount at a relative pressure P/P_0 of 0.99.

2.3. Electrochemical measurements

The electrochemical performances of the C@MoS_2 composites were evaluated with a coin-type half cells (CR 2025). The working electrodes were prepared by casting a slurry of 80 wt.% of the as-prepared active materials, 10 wt.% of Super-P carbon black, and 10 wt.% of poly(vinyl difluoride) (PVDF) in N-methyl-2-pyrrolidinone (NMP) on a copper foil. The coated electrodes were dried in vacuum at 110 °C for 12 h and then pressed with an active material loading of 1.0 mg cm^{-2}. Galvanostatic charge/discharge cycles of the cell were performed between cut-off potential of 0.005 and 3.0 V at room temperature (25 ± 1 °C) on a Land battery measurement system (LAND CT-2001A, Wuhan, China) at various current densities. The two-electrode cells were assembled in an argon-filled glovebox with the metallic lithium foil as both the reference and counter electrodes, a polypropylene membrane (Celgard-2300) as the separator, and 1.0 M $LiPF_6$ in a 1:1 v/v mixture of ethylene carbonate (EC) and dimethyl carbonate (DMC) as the electrolyte. Cyclic voltammetry (CV) was carried out on an electrochemical workstation (CHI 660D, Chenhua, Shanghai) in a voltage range of 0.005–3 V at a scan rate of 0.5 mV s^{-1}. Electrochemical impedance spectroscopy (EIS) results were obtained by applying a sine wave with an amplitude of 5.0 mV over the frequency ranging from 100 kHz to 0.01 Hz.

3. Results and discussion

Fig. 1 illustrates the fabrication process of C@MoS_2 composite. The C@MoS_2 composites were prepared by a hydrothermal reaction between sodium molybdate and thiourea with the aid of sucrose as a binder and MgO as a structure-directing agent. Specifically, commercial MgO powder could be easily transformed into hexagonal platelets of $Mg(OH)_2$ under hydrothermal treatment at 180 °C for 24 h [26–28]. As shown in Fig. S1a, the obtained $Mg(OH)_2$ by a hydrothermal recrystallization process exhibits typical hexagonal-shaped nanoplate morphology with a uniform size of 500 nm. More importantly, the $Mg(OH)_2$ nanoplate possesses a high specific surface area of 46.2 m^2 g^{-1} with a large amount of mesopores and macropores (Fig. S1b), exhibiting good adsorption performance [29]. Therefore, the molybdenum precursor (Na_2MoO_4) and the sulfur source (NH_2CSNH_2) could be successfully adsorbed within the pores of the $Mg(OH)_2$ nanoplates. Additionally, $Mg(OH)_2$ nanoplates with a positive zeta potential could easily interact with negative charged MoO_4^{2-} via strong electrostatic attraction [30]. Under the assistance of structure-directing agent of $Mg(OH)_2$ nanoplates, MoS_2 were naturally grown and spread along the surface and edge of the $Mg(OH)_2$ template. The synthetic reaction of MoS_2 can be described as follows [31]:

$$2NH_2CSNH_2 + 2H_2O \rightarrow 2NH_3 + H_2S + CO_2 \quad (1)$$

$$4MoO_4^{2-} + 9H_2S + 3CO_2 \rightarrow 4MoS_2 + SO_4^{2-} + 3CO_3^{2-} + 9H_2O \quad (2)$$

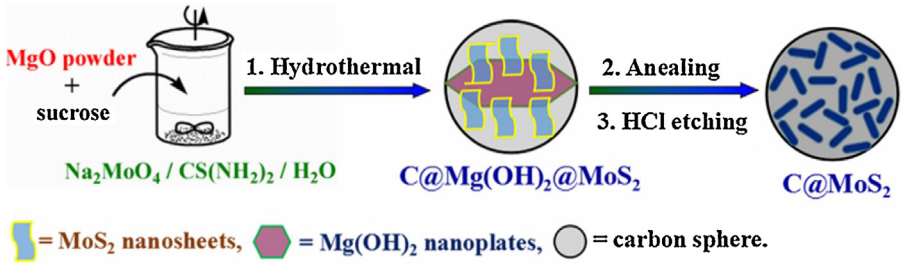

Fig. 1. Schematic illustration of the synthesis process of C@MoS_2 composite.

The hydrothermal products were then annealed in H_2/Ar atmosphere to carbonize the colloidal carbonaceous material derived from sucrose and crystallize the MoS_2 crystal. Meanwhile, the $Mg(OH)_2$ nanoplates were transformed into MgO after calcination. After treating the samples with HCl solution to remove the MgO templates, C@MoS_2 composites were obtained.

The morphologies of the as-prepared C@MoS_2-0 ~ C@MoS_2-3 composites are revealed by SEM. As shown in Fig. 2a, the template-free sample C@MoS_2-0 displays uneven, sphere-like agglomerated particles with diameter of several micrometers together with tiny particles on the surface. It is reported that sucrose-derived carbonaceous materials by a hydrothermal approach are sphere-like architectures [15]. TEM image of the MgO@amorphous carbon composite (Fig. S1c) further confirms the formation of carbon microspheres with highly porous structure and smooth surface by hydrothermal carbonization of sucrose. Thus, sucrose plays a key role in the formation of sphere-like morphology of C@MoS_2-0 composite in hydrothermal process. Similarly, both the C@MoS_2-1 and C@MoS_2-2 composites display typical 3D sphere-like morphology with rough surface (Fig. 2b and c). In detail, a large amount of uneven spherical particles can be observed for C@MoS_2-1 composite under low concentration of MgO template, while C@MoS_2-2 composite exhibits uniform spheres with a reduced diameter of 600–1000 nm under medium concentration. This suggests that the presence of an appropriate concentration of MgO template favors the MoS_2 and colloidal carbon to form uniform spheres. It is noteworthy that the surface of spheres are rather rough, which are constructed by worm-like, 1D nanorods with a diameter of 20–50 nm and a length of 80–150 nm (Fig. 2e and f). The construction of such unique nanoarchitecture can be attributed to an effective integration of sucrose as a binder and the $Mg(OH)_2$ nanoplates as a hard template. The creation of Mg $(OH)_2$ nanoplates by hdrothermal treatment can be further proved by the TEM image. As shown in Fig. S1d, a large number of MgO nanoplates are well distributed in the amorphous carbon network. More importantly, for C@MoS_2-2 composite, the loosely packed architecture and the void spaces between the neighboring MoS_2 nanorods might not only make it contact well with the electrolyte and provide more reactive sites for Li-ion intercalation, but also facilitate the rapid diffusion of lithium ions so that the active materials can be adequately utilized [9,20]. However, higher concentration of MgO template results in an irregular morphology of the C@MoS_2-3 composite (Fig. 2d). Only few worm-like nanorods can be found on its aggregated surface, due to the severe aggregation of MgO templates during hydrothermal treatment.

To further investigate the growth mechanism of the C@MoS_2-2 composite, the evolution process of the C@MoS_2-2 composite products collected at different times such as 1 h, 6 h, 15 h, and 24 h was studied by observing the sample morphology (Fig. S2 a-f). At the early stage (1 h), due to the short time of reaction, the product is composed of loosely packed particles with rough surface (Fig. S2a). When the reaction time is prolonged to 6 h, the little particles gradually grow into sphere-like aggregates and their surface consist of thin nanosheets under the assistance of MgO template during hydrothermal treatment (Fig. S2b, e). After increasing the reaction time to 15 h, the spherical particles are uniformly covered with flower-like nanosheets (Fig. S2c, f). After

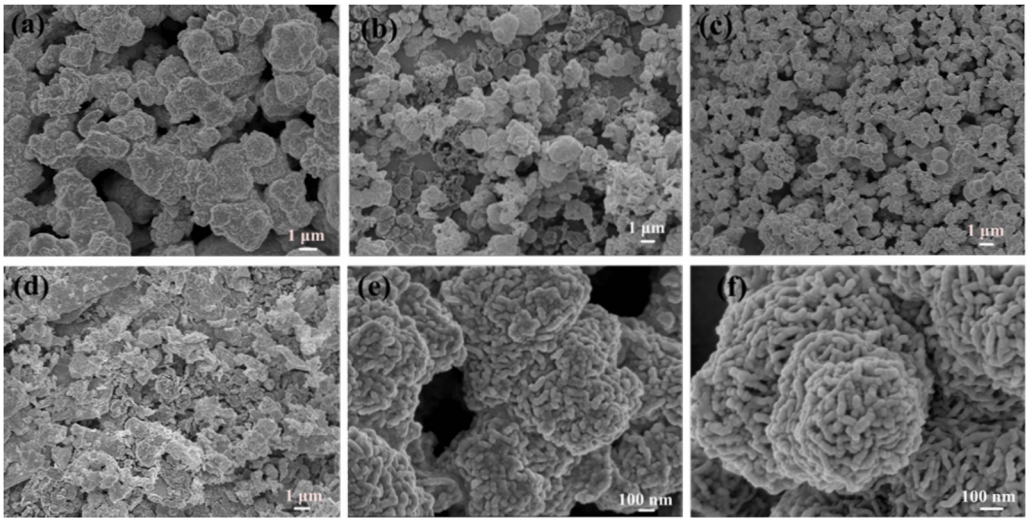

Fig. 2. SEM images of (a) C@MoS_2-0, (b, e) C@MoS_2-1, (c, f) C@MoS_2-2 in low and high magnifications, (d) C@MoS_2-3.

elongating to 24 h, thin nanosheets on the surface of the microspheres tend to disappear and then are transformed into worm-like nanorods as the building blocks and the main product (Fig. S2d). This could be attributed to the presence of $Mg(OH)_2$ nanoplates as the structure-directing agent, which could be favorable to the nucleation and growth of the nanorods.

More detailed surface morphologies and microstructures of the C@MoS_2 composites are further characterized by using TEM. Fig. 3a–d displays the layered MoS_2 crystals of C@MoS_2-0 ~ C@MoS_2-3 composites, which is homogeneously dispersed in amorphous carbon matrix. Compared with template-free C@MoS_2-0 composite, the introduction of the hard template in C@MoS_2 composites favors the formation of highly porous and well distributed MoS_2 nanosheets with few-layered structure. It is clearly observed that the C@MoS_2-2 composite exhibits relatively loose and uniform spheres with many edges (Fig. 3c), which is in accordance with the morphology observed in SEM. Such unique structure is considered to be beneficial for Li-ion insertion/extraction and electrolyte access, probably resulting in improved electrochemical performance. Fig. 3e shows that the bare MoS_2 possesses a well-defined layered structure (4-11 layers) with a lattice spacing of 0.62 nm, which corresponds to the inter-plane spacing of (002) plane of hexagonal MoS_2 [10,11]. Fig. 3f demonstrates the few-layered structure of the C@MoS_2-2 composite with 3-6 layers and an interlayer distance of 0.96 nm. Compared to that of the bare MoS_2, the enlarged $d_{(002)}$-space of MoS_2 nanosheets in C@MoS_2-2 composite affirms the existence of amorphous carbon between the layers of MoS_2, which is consistent with those of MoS_2/amorphous carbon composites prepared by glucose-assisted hydrothermal route [15,32]. A typical HRTEM image further confirms that the amorphous carbon layer (~0.85 nm) is uniformly wrapped on the few-layered MoS_2 nanosheets, resulting in a core-shell structured carbon@MoS_2 composite (Fig. S3a). The selected-area electron diffraction pattern of the C@MoS_2-2 composite (Fig. S3b) further proves the hexagonal phase of MoS_2.

The mass fraction of MoS_2 in C@MoS_2 composites is determined by thermogravimetric analysis in dry air (Fig. 4a). By assuming that the remaining residues after the TGA analysis is bare MoO_3 [33], the MoS_2 content in the C@MoS_2-0 and C@MoS_2-2 composites can be calculated to be approximately 82.2 and 81.4%, respectively. It suggests that the incorporation of MgO template into the synthetic

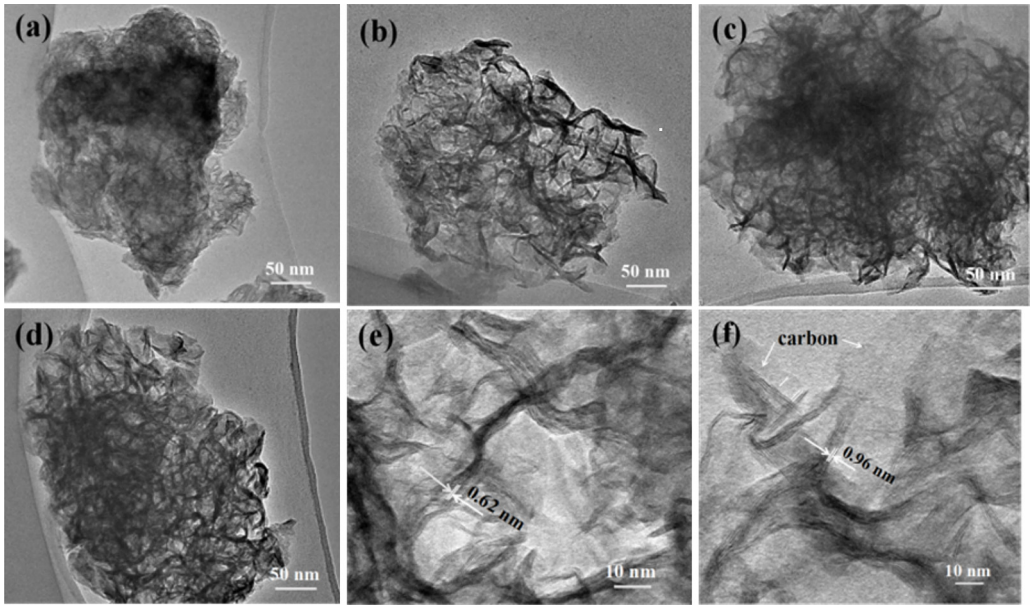

Fig. 3. TEM images of (a) C@MoS_2-0, (b) C@MoS_2-1, (c) C@MoS_2-2, (d) C@MoS_2-3, and HRTEM images of (e) bare MoS_2 and (f) C@MoS_2-2.

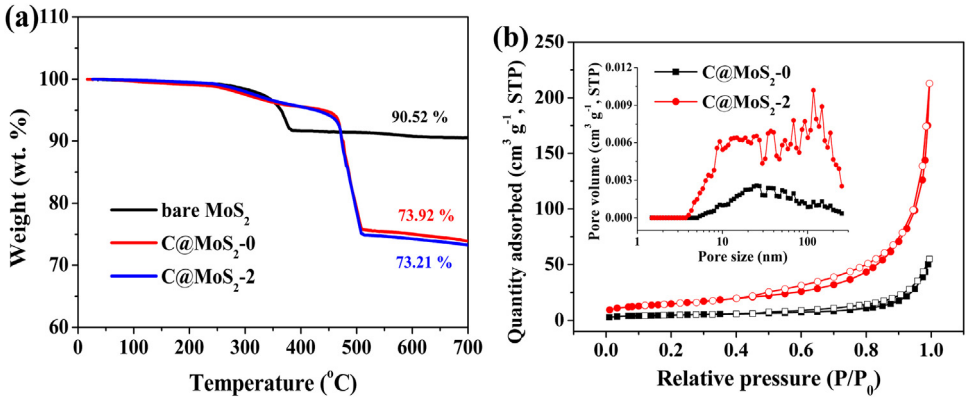

Fig. 4. (a) TG curves of the bare MoS_2, C@MoS_2-0 and C@MoS_2-2 composites under air atmosphere at a ramp rate of 10 °C min^{-1}. (b) N_2 adsorption-desorption isotherm and their corresponding pore size distribution curves of the C@MoS_2-0 and C@MoS_2-2 composites.

system has a negligible effect on the composition of C@MoS_2 composites.

The porous structure of the C@MoS_2 composites is also characterized by nitrogen adsorption/desorption isotherms, and the specific surface area is obtained by the BET method. As shown in Fig. 4b, both the C@MoS_2-0 and C@MoS_2-2 composites exhibit very similar type IV isotherm and H3 hysteresis loop, indicating the presence of mesopores [31,34]. Moreover, compared with C@MoS_2-0 composite, there is a noticeable increase of N_2 adsorption for the C@MoS_2-2 composite, implying the generation of pores due to the introduction of MgO template. The BET surface area of C@MoS_2-2 composite was measured to be 52.7 $m^2 g^{-1}$ with a pore volume of 0.16 $cm^3 g^{-1}$, which is much higher than that of C@MoS_2-0 composite (16.9 $m^2 g^{-1}$). The pore size distributions obtained by density functional theory further confirm that both C@MoS_2-0 and C@MoS_2-2 composites possess a hierarchically porous structure with meso-/macropores from 5 to 250 nm (inset of Fig. 4b). Such highly porous structure with large surface area for C@MoS_2-2 composite could facilitate Li^+ diffusion at the electrolyte-electrode interface and greatly alleviate the volume expansion of MoS_2 during discharge/charge process [7,35].

Fig. 5a shows the XRD patterns of the bare MoS_2. The bare MoS_2 displays sharp diffraction peaks at $2\theta = 14.4°$, 33.9°, 40.1°, 59.7°, and 69.7°, which agrees well with the standard peaks of the hexagonal MoS_2 phase (JCPDS card No. 37-1492). Remarkably, the strong peak at 14.4°, which can be assigned to the (002) plane of the 2-H MoS_2, indicates the existence of well-stacked layered structure [36]. Fig. 5b displays the XRD patterns of the C@MoS_2-0 ~ C@MoS_2-3 composites. The weak and broad diffraction peaks at 15°–26° correspond to the (002) plane of amorphous carbon materials [15,37]. Two diffraction peaks at $2\theta = 33.3°$ and 58.9° can be attributed to the (100) and (110) planes of MoS_2. Compared with bare MoS_2, the absence of (002) plane of MoS_2 for C@MoS_2-0 ~ C@MoS_2-3 composites is indicative of few-layer structure [38], which is in accordance with their TEM observations. It also implies that the incorporation of sucrose-derived amorphous carbon into the composite could effectively suppress the (002) plane growth of MoS_2 crystal [32]. Therefore, sucrose-derived carbon in C@MoS_2 composites not only serve as a good conducting network for MoS_2, but also acted as a spacer agent to form few-layered MoS_2 structure [39,40].

The Raman spectroscopy has been proved to be a useful characterization tool to investigate different crystalline structures of MoS_2 [41,42]. Fig. 5c shows the Raman spectra of the bare MoS_2, C@MoS_2-0, and C@MoS_2-2 composites. The Raman spectra of the bare MoS_2 shows two sharp peaks at 381 and 408 cm^{-1}, which can be attributed to the $E_{2g}{}^1$ and A_{1g} modes of the hexagonal MoS_2 crystal, respectively [43]. The $E_{2g}{}^1$ mode is related to the in-layer displacement of Mo and S atoms, whereas the A_{1g} mode results from the out-of-layer symmetric displacement of S atoms along the c axis [39]. Remarkably, as shown in Fig. 5d, these two Raman peaks of C@MoS_2-0 and C@MoS_2-2 are much weaker and broader than that of bare MoS_2, implying the presence of few-layered structure owing to the phonon confinement [44]. Moreover, the $A^1{}_g$ peaks of these two composites shifted down to 404 cm^{-1}. According to previous reports, the $A^1{}_g$ peak of the MoS_2 would shift toward low wavenumber when the layer number is less than six [32,44]. Therefore, it can be inferred that the incorporation of sucrose as the carbon source into the MoS_2 interlayers leads to the blue-shift of the $A^1{}_g$ mode in comparison with that of bare MoS_2, which is related to the formation of few-layered MoS_2 in two C@MoS_2 composites. These results well agree with the XRD and TEM analyses. In addition, the Raman spectra of C@MoS_2-0 and C@MoS_2-2 composites display two new, dominant peaks at 1364

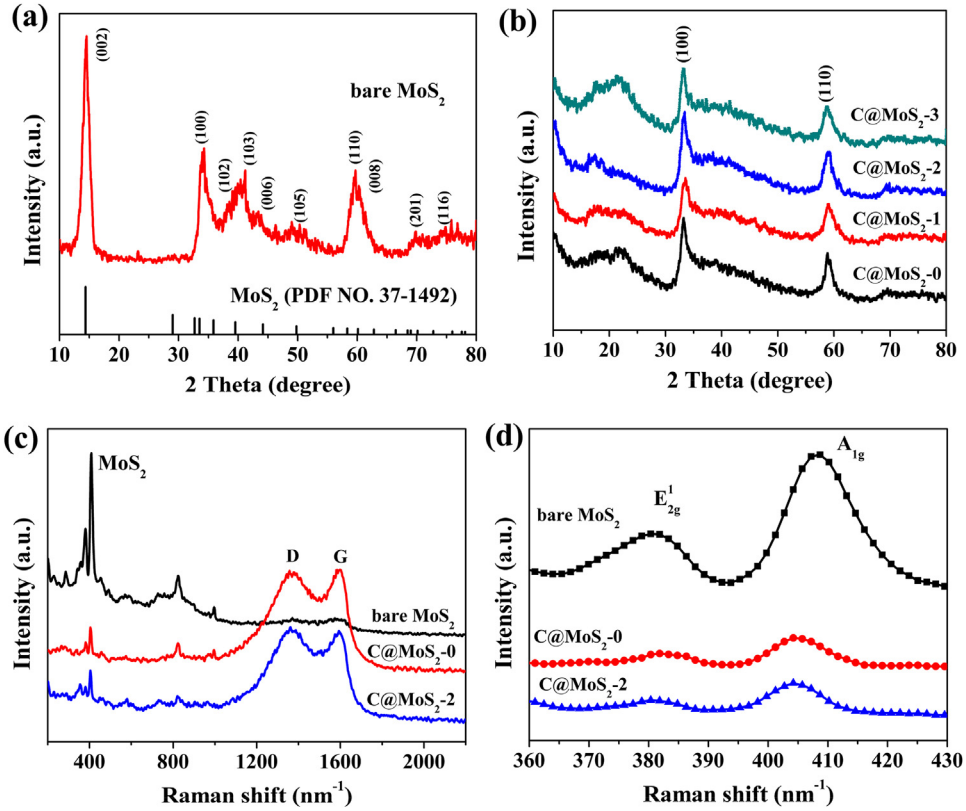

Fig. 5. XRD patterns of (a) the bare MoS_2, and (b) C@MoS_2-0 ~ C@MoS_2-3 composites. (c) Raman spectra and (d) partial magnified Raman spectra of the bare MoS_2, C@MoS_2-0 and C@MoS_2-2 composites.

and 1595 cm^{-1}, which belong to the D and G bands of carbon materials, respectively [45]. It indicates the existence of carbon materials in C@MoS_2 composites, which is well consistent with the XRD result. The D band corresponds to the structure defects and disorder sp^3 carbon atoms in graphite layers, while the G band is associated with the stretching vibration of sp^2 hybridized carbon atoms in 2D hexagonal lattice [46]. The relative intensity ratio between D and G bands (I_D/I_G) reveals the graphitic degree of the carbonaceous materials [47]. By comparing the Raman spectra of C@MoS_2-0 and C@MoS_2-2, the slight increase of the I_D/I_G from 0.99 to 1.04 reflects a more defective structure in C@MoS_2-2 composite. It might be due to its porous architecture for C@MoS_2-2 composite caused by the introduction of MgO template. On the whole, both two C@MoS_2 composites have a high graphitic degree of carbon matrix, which is considered to be beneficial for the enhancement of electrical conductivity.

Fig. 6 shows the initial five CV curves of the bare MoS_2 and C@MoS_2-2 electrodes. In the first cathodic scan, two pronounced reduction peaks are clearly observed, namely: ~0.75 and 0.30 V for the bare MoS_2 electrode, and ~0.68 and 0.42 V for C@MoS_2-2 electrode (Fig. 6a and b). The plateau at 0.68-0.75 V can be assigned to the formation of Li_xMoS_2, leading to a phase transformation of MoS_2 from trigonal prismatic (2H) to octahedral (1T) structure [31]. The other plateau at 0.30-0.42 V corresponds to the conversion reaction in which MoS_2 decomposes into Mo particles that embedded in a Li_2S matrix. In the subsequent lithiation cycles, the two peaks at 0.68-0.75 and 0.30-0.42 V disappear. Instead, two new peaks arise at about 1.70 and 0.40 V, indicating a multistep lithium insertion mechanism based on the following conversion reactions (reactions (3)–(5)) [8]:

$$MoS_2 + xLi^+ + xe^- \rightarrow Li_xMoS_2 \quad (3)$$

$$MoS_2 + 4Li \rightarrow Mo + 2Li_2S \quad (4)$$

$$Li_xMoS_2 + (4-x)e^- + (4-x)Li^+ \rightarrow Mo + Li_2S \qquad (x = 1-4) \quad (5)$$

For the bare MoS_2, the shifts in the reduction potentials and the changes in the reduction peak shape after the first cycle might be attributed to its poor structural stability with well-stacked layered architecture [37]. In the first anodic scan, a pronounced peak at 2.33-2.40 V can be clearly identified, which is ascribed to the oxidation of Li_2S to sulfur and lithium ions [36]. In the subsequent cycles, the oxidation peak at 2.40 V for the bare MoS_2 electrode becomes much weaker and exhibits a shift toward the high voltage, implying the poor structure stability of bare MoS_2 electrode. As for C@MoS_2-2 electrode, the prominent oxidation peaks at 2.33 V coupled with several small oxidation peaks at 1.0-1.7 V resulting from the incomplete oxidation of Mo particles are visible in the first and second anodic scan [32]. In the successive cycles, these weak oxidation peaks at 1.0-1.7 V disappear, while its CV shape and the oxidation peaks at 2.33 V can still maintain, suggesting good stability and reversibility.

Fig. 7 shows the initial galvanostatic charge/discharge profiles of the C@MoS_2 composite electrodes at a current density of 100 mA g^{-1} with a cutoff voltage window of 0.005-3.0 V. The C@MoS_2-0 ~ C@MoS_2-3 composite electrodes exhibit inconspicuous potential plateaus at 1.1-1.4 V and 0.6 V in the first discharge (lithiation) process (Fig. 7a–d). The plateau at 1.1-1.4 V can be attributed to the insertion of lithium ions into the interlayer space of MoS_2 to form Li_xMoS_2, whereas the plateau at 0.6 V is indicative of a conversion reaction process, in which Li_xMoS_2 is decomposed to Mo particles and Li_2S [16,22]. For the second and fifth cycles, all C@MoS_2 composite electrodes display three inconspicuous potential plateaus at around 2.0, 1.2 and 0.3 V, which are in good accordance with the corresponding changes of their CV curves. In the charge (delithiation) process, these C@MoS_2 composite electrodes show an obvious potential plateaus at 2.2 V for the first and subsequent cycles, corresponding to their oxidation peaks at 2.3-2.4 V in their CVs [48]. According to their first cycles, the initial specific discharge capacities of the C@MoS_2-0, C@MoS_2-1, C@MoS_2-2, and C@MoS_2-3 composite electrodes are calculated to be 835.3, 1109.6, 1513.6, and 1035.4 mAh g^{-1} (based on the total weight of the composites), respectively. Correspondingly, their charge capacities are 671.6, 874.6, 1118.8, and 765.7 mAh g^{-1} with Coulombic efficiency (CE) of 80.4, 78.8, 73.9, and 74.0%, respectively. The irreversible capacity loss in the first cycle can be ascribed to the formation of solid-electrolyte interphase (SEI) film [36,38] and the utilization of sucrose-derived amorphous carbon, whose CE is as low as 49.1% (Fig. S4a, c). Although the bare MoS_2 electrode initially delivers a slightly higher capacity of 842.8 mAh g^{-1}, its reversible capacity drops rapidly with the cycle number (Fig. S4b, d). Compared with bare MoS_2 and amorphous carbon, the significantly enhanced reversible capacity for the C@MoS_2 composite electrodes can be caused by the combined effects of the MoS_2 nanosheets and the porous carbon spheres (Fig. S1c).

Remarkably, among all samples, C@MoS_2-2 composite electrode delivers the highest initial discharge and charge capacities. Obviously, the morphology and structure of C@MoS_2 composites synthesized with different amount of MgO template has a substantial influence on their electrochemical performances. In comparison with uneven spherical particles of C@MoS_2-0 and C@MoS_2-1 with low surface area as well as C@MoS_2-3 aggregates with irregular morphology, the uniform sphere-like C@MoS_2-2

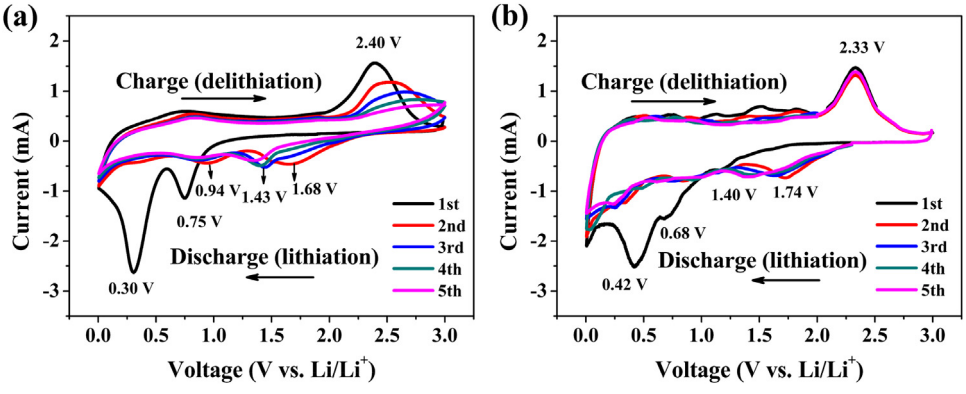

Fig. 6. Cyclic voltammograms at a scan rate of 0.5 mV s^{-1}: (a) the bare MoS_2 and (b) C@MoS_2-2 composite electrode.

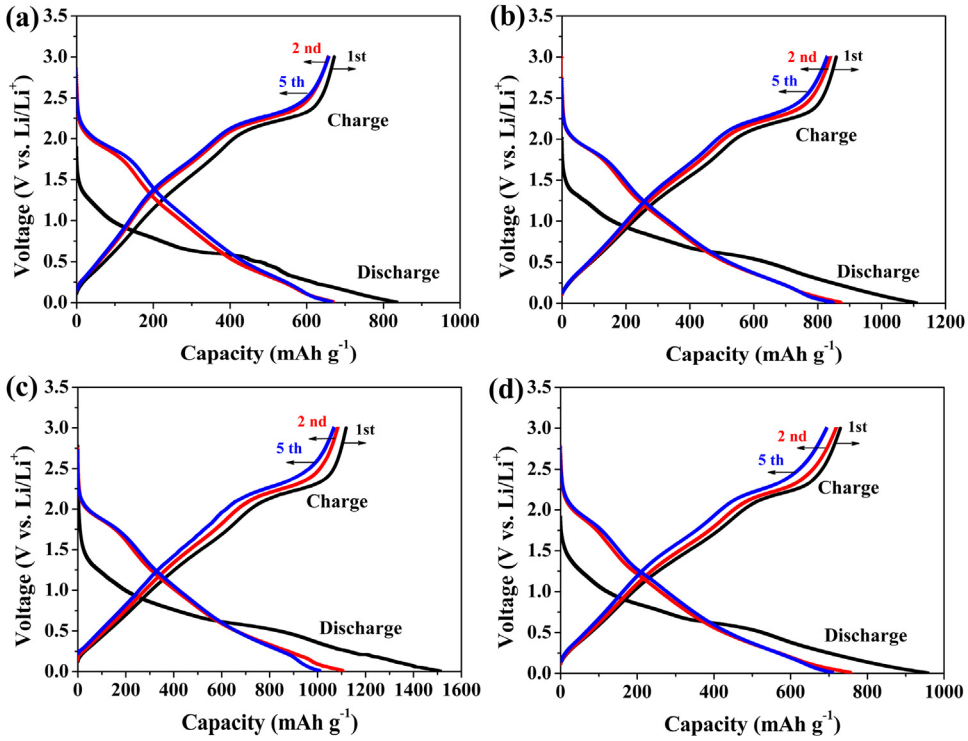

Fig. 7. Charge-discharge potential profiles of the C@MoS_2 composite electrodes: (a) C@MoS_2-0, (b) C@MoS_2-1, (c) C@MoS_2-2, (d) C@MoS_2-3 at a current density of 100 mA g^{-1}.

composite with large surface area and hierarchical architecture favors the enhancement of the lithium storage capacity. The slightly lower CE for C@MoS_2-2 composite than those of other C@MoS_2 composites is probably due to its more defective carbon matrix for trapping the lithium. After the first cycle, the CE for the four electrodes soar to more than 95.0%.

The cycling stability of the bare MoS_2, C@MoS_2-0, and C@MoS_2-2 composite electrodes at various current densities from 100 to 5000 mA g^{-1} are plotted in Fig. 8a. The cyclic stability of the bare

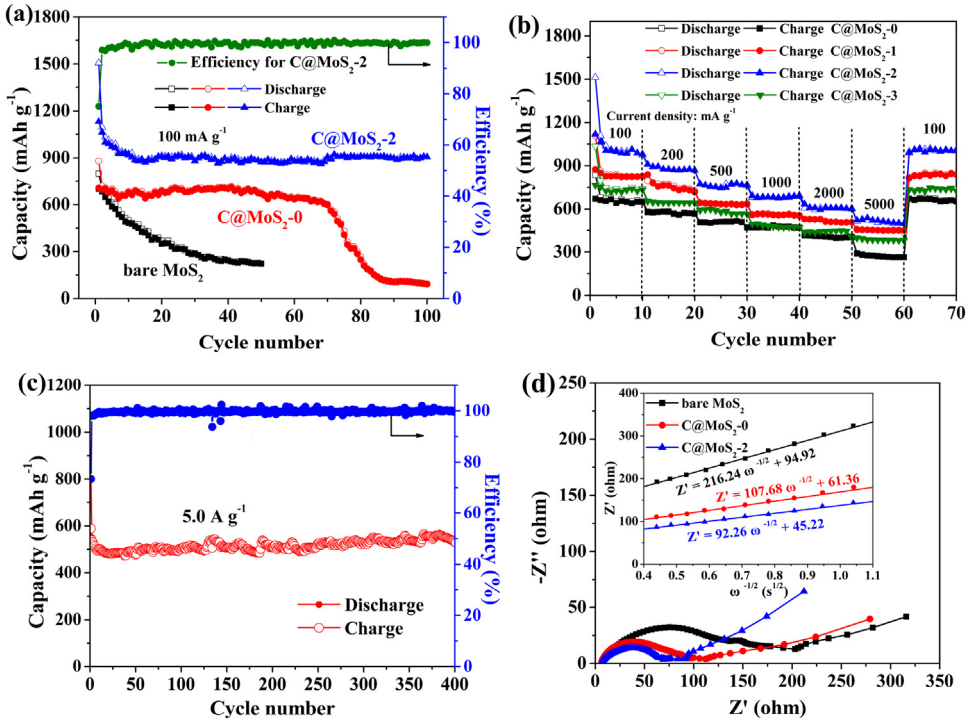

Fig. 8. (a) Cycle performances of the bare MoS_2, C@MoS_2-0, and C@MoS_2-2 composite at a current density of 100 mA g^{-1}. (b) rate capabilities of C@MoS_2-0 ~ C@MoS_2-3 composites at different current densities. (c) cycling performance of the C@MoS_2-2 composite electrode at a current density of 5.0 A g^{-1} and its corresponding Coulombic efficiency. (d) Nyquist plots (the inset graph of Z′ plotted against $\omega^{-1/2}$ at the low frequency) of the bare MoS_2, C@MoS_2-0 and C@MoS_2-2 composite electrodes.

MoS_2 is so poor that the reversible capacity continuously decreases with cycle number, delivering a low capacity retention of ~27.8% after 50 cycles. The poor cyclability of the bare MoS_2 electrode is mainly associated with its severe self-restacked structure and low electrical conductivity. In contrast, both the C@MoS_2-0 and C@MoS_2-2 composites possess more stable cycle stability and higher reversible capacities than that of bare MoS_2. This further demonstrates that the combination of amorphous carbon and MoS_2 would lead to a remarkable synergy effect in reversible lithium storage. However, when the cycle number increases up to 70, the C@MoS_2-0 composite displays a fast and successive decay in capacity. It might be ascribed to its electrode pulverization caused by the large strain derived from huge volume change during repeated lithiation/delithiation processes. Moreover, low specific surface area with low porosity and the agglomerated particles without any voids for C@MoS_2-0 composite also lead to continuous capacity loss. As for C@MoS_2-2 composite, it exhibits a significantly improved cyclic stability in comparison with bare MoS_2 and C@MoS_2-0 electrodes. Even after 100 cycles, the reversible capacity of the C@MoS_2-2 composite still retains at about 905.3 mAh g^{-1} with a high capacity retention of 82.7% when compared to the second cycle. As shown in Fig. S5, it was found that C@MoS_2-2 composite still maintained sphere-like morphology, except that its highly porous architecture became denser probably due to the large volume expansion during cycling.

Even at a high current density of 5.0 A g^{-1}, the C@MoS_2-2 composite also can deliver a high reversible capacity of 503.9 mAh g^{-1} with a capacity retention of 93.4% and a CE of ~99.7% after 400 cycles, suggesting an outstanding high-rate stability (Fig. 8c). Such outstanding cycling stability of C@MoS_2-2 composite can be ascribed to its hierarchical nanostructure with large surface area to buffer the large volume expansion upon the lithiation process and the conductive carbon network as the skeleton to ensure the structural stability. It is worth mentioning that such high reversible capacity and capacity retention of C@MoS_2-2 electrode are much better or comparable with those of MoS_2-based electrodes reported previously (Table S1).

Rate capability is of substantial significance in practical applications of LIBs. The rate capabilities of the C@MoS_2-0 ~ C@MoS_2-3 composite electrodes at different current densities are also evaluated, as shown in Fig. 8b. It can be clearly observed that among the four C@MoS_2 composites, C@MoS_2-2 composite delivers the highest reversible capacities of 1012.5, 876.0, 774.3, 682.1, 603.5, and 503.4 mAh g^{-1} at current densities of 100, 200, 500, 1000, 2000, and 5000 mA g^{-1}, respectively. Noticeably, when the current density is returned back to 100 mA g^{-1} after cycling under high current densities, C@MoS_2-2 composite can still regain a reversible capacity of 1004.6 mAh g^{-1}. In contrast, the amorphous carbon, bare MoS_2, and template-free C@MoS_2-0 composite can only deliver much lower capacities of 95.2, 52.9, and 263.7 mAh g^{-1} at 5000 mA g^{-1}, respectively (Figs. 8b, S3c, and S3d). The greatly enhanced rate performance of the C@MoS_2-2 composite is closely associated with the following factors: (1) its large surface area to provide sufficient electrode/electrolyte contact and more exposed active sites; (2) the expanded MoS_2 interlayer to facilitate fast diffusion of lithium ions; (3) a hierarchically porous structure to accommodate the volume change during the lithiation/delithiation process; (4) the amorphous carbon as the conductive matrix in the composite to ensure fast electron transport [49].

In order to better understand the excellent electrochemical performance of C@MoS_2-2 composite in comparison with other samples, the electrochemical impedance spectroscopy (EIS) was performed to study the electrochemical reaction kinetics of the bare MoS_2, C@MoS_2-0, and C@MoS_2-2 composite electrodes after ten cycles, as shown in Fig. 8d. It can be seen that, for C@MoS_2-2 electrode, the diameter of the semicircle in the high-/medium frequency is the smallest among three electrodes, implying that C@MoS_2-2 composite possesses the lowest contact resistance and charge-transfer resistance for the insertion/extraction reactions [31,50]. It can be attributed to the incorporation of conductive carbon matrix and the unique nanostructure with self-assembled nanorods. Besides, the straight line in the low frequency region in the Nyquist plots is indicative of Warburg behavior arising from the diffusion of lithium ions in the electrode [51–53]. The C@MoS_2-2 composite electrode shows a steeper straight line in the low frequency region than those of bare MoS_2 and C@MoS_2-0 electrodes, indicating a lower diffusion impedance. The lithium ion diffusion coefficient in these electrodes can be calculated from the following formula [54]:

$$D_{Li^+} = \frac{1}{2}\left[\left(\frac{RT}{An^2CF^2}\right)\frac{\partial w^{-\frac{1}{2}}}{\partial Z'}\right]^2 \quad (6)$$

where D_{Li^+} is the lithium ion diffusion coefficient ($cm^2\,S^{-1}$), A is the surface area of the electrode ($1.13 \times 10^{-4}\,m^2$), n is the number of the electrons per MoS_2 molecule attending the electronic transfer reaction (n is 4), C is the molar concentration of Li^+ in electrolyte ($1.20 \times 10^4\,mol\,m^{-3}$), F is the Faraday constant (96486C mol^{-1}), R is the gas constant (8.314 J $mol^{-1}\,K^{-1}$), T is the absolute temperature (298 K), Z′ is the real Warburg resistance and ω is the angular frequency in low frequency region. The lithium ion diffusion coefficient D_{Li^+} of the bare MoS_2, C@MoS_2-0 and C@MoS_2-2 composite electrodes calculated by Eq. (6) from the slope of ($\partial\omega^{-1/2}/\partial Z'$) (inset of Fig. 8d) were 1.61×10^{-18}, 6.48×10^{-17}, and $8.82 \times 10^{-17}\,cm^2\,S^{-1}$, respectively. Obviously, the C@MoS_2-2 composite electrode exhibited the largest lithium ion diffusion coefficient after 10 cycles among these three electrodes. It further proves that the worm-like nanorods assembled structure of C@MoS_2-2 composite not only effectively provides more active sites, shortens the diffusion paths of lithium ions and electrolyte, but also facilitates the easy access of the lithium ions. As a result, C@MoS_2-2 composite exhibits greatly improved lithium ion kinetics in the electrode materials and enhanced rate capability when compared to the bare MoS_2, and C@MoS_2-0 composite.

By and large, the C@MoS_2-2 composite shows the superior lithium storage performance with high reversible capacity, outstanding rate capability, and long cycle life. It can be accounted for by considering the following aspects: firstly, the conductive carbon backbone not only prevents the restacking and aggregation of MoS_2 nanosheets during cycling, simultaneously enlarges the interlayer distance of MoS_2 nanosheets to accommodate more Li^+, but also improves the electrical conductivity of electroactive MoS_2; secondly, the large surface area and self-assembled worm-like nanostructure provides substantial active sites for hosting lithium ions, and facilitates the fast transportation of Li^+ and the electrolyte, leading to an improved kinetic performance of the reversible lithium storage; thirdly, the hierarchically porous architecture and sufficient void space between the nanorods are beneficial for buffering the large volume expansion during the repeated charge/discharge process, which is favorable for improvement of the cycling stability of the MoS_2-based electrode.

4. Conclusions

In summary, a novel 3D sphere-like C@MoS_2 composite which consisted of 1D worm-like nanorods was successfully fabricated by a one-pot hydrothermal method with the assistance of commercial MgO powder as a hard template followed by a annealing treatment. Morphology and structure of the C@MoS_2 composites could be easily tailored by changing the concentration of MgO template. The C@MoS_2 composite electrode delivered a

maximum reversible capacity of 905.3 mAh g^{-1} at a current density of 100 mA g^{-1}, excellent rate capability (503.4 mAh g^{-1} at 5000 mA g^{-1}), and superior cycling performance (503.9 mAh g^{-1} after 400 cycles at 5000 mA g^{-1}). Such outstanding lithium storage performance for C@MoS_2-2 composite could be attributed to its unique hierarchical nanostructure with large surface area and synergetic effect between few-layered MoS_2 and amorphous carbon. More importantly, our approach provides a facile and scalable strategy for the synthesis of the C@MoS_2 composite anode material for high-performance LIBs.

Acknowledgement

None.

Appendix A. Supplementary data

Supplementary data associated with this article can be found, in the online version, at http://dx.doi.org/10.1016/j.electacta.2016.06.115.

References

[1] P.G. Bruce, B. Scrosati, J.M. Tarascon, Nanomaterials for Rechargeable Lithium Batteries, Angew. Chem. Int. Ed. 47 (2008) 2930.
[2] N. Recham, J.N. Chotard, L. Dupont, C. Delacourt, W. Walker, M. Armand, J.M. Tarascon, A 3.6 V Lithium-Based Fluorosulphate Insertion Positive Electrode for Lithium-Ion Batteries, Nat. Mater. 9 (2009) 68.
[3] B. Kang, G. Ceder, Battery Materials for Ultrafast Charging and Discharging, Nature 458 (2009) 190.
[4] K.T. Nam, D.W. Kim, P.J. Yoo, C.Y. Chiang, N. Meethong, P.T. Hammond, Y.M. Chiang, A.M. Belcher Virus-Enabled Synthesis and Assembly of Nanowires for Lithium Ion Battery Electrodes, Science 312 (2006) 885.
[5] M. Armand, J.M. Tarascon, Building Better Batteries, Nature 451 (2008) 652.
[6] K. Kang, Y.S. Meng, J. Breger, C.P. Grey, G. Ceder, Electrodes with High Power and High Capacity for Rechargeable Lithium Batteries, Science 311 (2006) 977.
[7] G.D. Du, Z.P. Guo, S.Q. Wang, R. Zeng, Z.X. Chen, H.K. Liu, Superior Stability and High Capacity of Restacked Molybdenum Disulfide as Anode Material for Lithium Ion Batteries, Chem. Commun. 46 (2010) 1106.
[8] P.P. Wang, H. Sun, Y. Ji, W. Li, X. Wang, Three-Dimensional Assembly of Single-Layered MoS_2, Adv. Mater. 26 (2014) 964.
[9] X. Hu, W. Zhang, X. Liu, Y. Mei, Y. Huang, Nanostructured Mo-Based Electrode Materials for Electrochemical Energy Storage, Chem. Soc. Rev. 44 (2015) 2376.
[10] C. Zhu, X. Mu, P.A. Van Aken, Y. Yu, J. Maier, Single-Layered Ultrasmall Nanoplates of MoS_2 Embedded in Carbon Nanofibers with Excellent Electrochemical Performance for Lithium and Sodium Storage, Angew. Chem. Int. Ed. 53 (2014) 2152.
[11] C. Zhu, X. Mu, P.A. Van Aken, J. Maier, Y. Yu, Fast Li Storage in MoS_2-Graphene-Carbon Nanotube Nanocomposites: Advantageous Functional Integration of 0D, 1D, and 2D Nanostructures, Adv. Energy Mater. 5 (2015) 1401170.
[12] J. Wang, J. Liu, J. Luo, P. Liang, D. Chao, L. Lai, J. Lin, Z. Shen, MoS_2 Architectures Supported on Graphene Foam/Carbon Nanotube Hybrid Films: Highly Integrated Frameworks with Ideal Contact for Superior Lithium Storage, J. Mater. Chem. A 3 (2015) 17534.
[13] K. Chang, W. Chen, L-Cysteine-Assisted Synthesis of Layered MoS_2/Graphene Composites with Excellent Electrochemical Performances for Lithium Ion Batteries, ACS Nano 5 (2011) 4720.
[14] Y. Shi, Y. Wang, J.L. Wong, A.Y.S. Tan, C.L. Hsu, L.J. Li, Y.C. Lu, H.Y. Yang, Self-Assembly of Hierarchical MoS_x/CNT Nanocomposites ($2 < x < 3$): Towards High Performance Anode Materials for Lithium Ion Batteries, Sci. Rep. 3 (2014) 2169.
[15] K. Chang, W. Chen, L. Ma, H. Li, H. Li, F. Huang, Z. Xu, Q. Zhang, J. Lee, Graphene-Like MoS_2/Amorphous Carbon Composites with High Capacity and Excellent Stability as Anode Materials for Lithium Ion Batteries, J. Mater. Chem. 21 (2011) 6251.
[16] S. Zhang, X. Yu, H. Yu, Y. Chen, P. Gao, C. Li, C. Zhu, Growth of Ultrathin MoS_2 Nanosheets with Expanded Spacing of (002) Plane on Carbon Nanotubes for High-Performance Sodium-Ion Battery Anodes, ACS Appl. Mater. Interfaces 6 (2014) 21880.
[17] C. Zhang, Z. Wang, Z. Guo, X.W. Lou, Synthesis of MoS_2-C One-Dimensional Nanostructures with Improved Lithium Storage Properties, ACS Appl. Mater. Interfaces 4 (2012) 3765.
[18] H. Hwang, H. Kim, J. Cho, MoS_2 Nanoplates Consisting of Disordered Graphene-like Layers for High Rate Lithium Battery Anode Materials, Nano Lett. 11 (2011) 4826.
[19] X.Y. Yu, H. Hu, Y. Wang, H. Chen, X.W. Lou, Ultrathin MoS_2 Nanosheets Supported on N-doped Carbon Nanoboxes with Enhanced Lithium Storage and Electrocatalytic Properties, Angew. Chem. Int. Ed. 54 (2015) 7395.
[20] D. Kong, H. He, Q. Song, B. Wang, W. Lv, Q.H. Yang, L. Zhi, Rational Design of MoS_2@Graphene Nanocables: Towards High Performance Electrode Materials for Lithium Ion Batteries, Energy Environ. Sci. 7 (2014) 3320.
[21] Z. Bai, Y. Zhang, Y. Zhang, C. Guo, B. Tang, Hierarchical MoS_2@Carbon Microspheres as Advanced Anodes for Li-Ion Batteries, Chem. Eur. J. 21 (2015) 18187.
[22] T. Stephenson, Z. Li, B. Olsen, D. Mitlin, Lithium Ion Battery Applications of Molybdenum Disulfide (MoS_2) Nanocomposites, Energy Environ. Sci. 7 (2014) 209.
[23] X. Xu, Z. Fan, S. Ding, D. Yu, Y. Du, Fabrication of MoS_2 Nanosheet@TiO_2 Nanotube Hybrid Nanostructures for Lithium Storage, Nanoscale 6 (2014) 5245.
[24] B. Guo, K. Yu, H. Fu, Q. Hua, R. Qi, H. Lin, H. Song, S. Guo, Z. Zhu, Firework-Shaped TiO_2 Microspheres Embedded with Few-Layer MoS_2 as an Anode Material for Excellent Performance Lithium-Ion Batteries, J. Mater. Chem. A 3 (2015) 6392.
[25] J. Jin, B. Kim, M. Kim, N. Park, S. Kang, S.M. Lee, H.J. Kim, S.U. Son, Template Synthesis of Hollow MoS_2-Carbon Nanocomposites Using Microporous Organic Polymers and Their Lithium Storage Properties, Nanoscale 7 (2015) 11280.
[26] J.C. Yu, A. Xu, L. Zhang, R. Song, L. Wu, Synthesis and Characterization of Porous Magnesium Hydroxide and Oxide Nanoplates, J. Phys. Chem. B 108 (2004) 64.
[27] L. Yan, J. Zhang, X. Sun, Z. Deng, Y. Li, Formation of Rod-Like $Mg(OH)_2$ Nanocrystallites Under Hydrothermal Conditions and the Conversion to MgO Nanorods by Thermal Dehydration, Mater. Chem. Phys. 76 (2002) 119.
[28] H. Pang, G. Wang, W. Gong, J. Ye, Y. Lin, Direct Synthesis of Hexagonal $Mg(OH)_2$ Nanoplates From Natural Brucite Without Dissolution Procedure, Chem. Commun. 47 (2011) 6317.
[29] L. Ai, H. Yue, J. Jiang, Sacrificial Template-Directed Synthesis of Mesoporous Manganese Oxide Architectures with Superior Performance for Organic Dye Adsorption, Nanoscale 4 (2012) 5401.
[30] J. Yan, Q. Wang, T. Wei, L. Jiang, M. Zhang, X. Jing, Z. Fan, Template-Assisted Low Temperature Synthesis of Functionalized Graphene for Ultrahigh Volumetric Performance Supercapacitors, ACS Nano 8 (2014) 4720.
[31] J. Wang, J. Liu, D. Chao, J. Yan, J. Lin, Z.X. Shen, Self-Assembly of Honeycomb-like MoS_2 Nanoarchitectures Anchored into Graphene Foam for Enhanced Lithium-Ion Storage, Adv. Mater. 26 (2014) 7162.
[32] G. Huang, T. Chen, W. Chen, Z. Wang, K. Chang, L. Ma, F. Huang, D. Chen, J. Lee, Graphene-Like MoS_2/Graphene Composites: Cationic Surfactant-Assisted Hydrothermal Synthesis and Electrochemical Reversible Storage of Lithium, Small 9 (2013) 3693.
[33] F. Sun, Y. Wei, J. Chen, D. Long, L. Ling, Y. Li, J. Shi, Melamine-Assisted One-Pot Synthesis of Hierarchical Nitrogen-Doped Carbon@MoS_2 Nanowalled Core-Shell Microspheres and Their Enhanced Li-Storage Performances, Nanoscale 7 (2015) 13043.
[34] Y. Tang, D. Wu, Y. Mai, H. Pan, J. Cao, C. Yang, F. Zhang, X. Feng, A Two-Dimensional Hybrid with Molybdenum Disulfide Nanocrystals Strongly Coupled on Nitrogen-Enriched Graphene via Mild Temperature Pyrolysis for High Performance Lithium Storage, Nanoscale 6 (2014) 14679.
[35] H. Jiang, D. Ren, H. Wang, Y. Hu, S. Guo, H. Yuan, P. Hu, L. Zhang, C. Li, 2D Monolayer MoS_2-Carbon Interoverlapped Superstructure: Engineering Ideal Atomic Interface for Lithium Ion Storage, Adv. Mater. 27 (2015) 3687.
[36] J. Zhou, J. Qin, X. Zhang, C. Shi, E. Liu, J. Li, N. Zhao, C. He, 2D Space-Confined Synthesis of Few-Layer MoS_2 Anchored on Carbon Nanosheet for Lithium-Ion Battery Anode, ACS Nano 9 (2015) 3837.
[37] S. Hu, W. Chen, J. Zhou, F. Yin, E. Uchaker, Q. Zhang, G. Cao, Preparation of Carbon Coated MoS_2 Flower-Like Nanostructure with Self-Assembled Nanosheets as High-Performance Lithium-Ion Battery Anodes, J. Mater. Chem. A 2 (2014) 7862.
[38] L. Ma, J. Ye, W. Chen, D. Chen, J.Y. Lee, Gemini Surfactant Assisted Hydrothermal Synthesis of Nanotile-Like MoS_2/graphene Hybrid with Enhanced Lithium Storage Performance, Nano Energy 10 (2014) 144.
[39] S. Ding, J.S. Chen, X.W. Lou, Glucose-Assisted Growth of MoS_2 Nanosheets on CNT Backbone for Improved Lithium Storage Properties, Chem. Eur. J. 17 (2011) 13142.
[40] J. Wang, C. Luo, T. Gao, A. Langrock, A.C. Mignerey, C. Wang, An Advanced MoS_2/Carbon Anode for High-Performance Sodium-Ion Batteries, Small 4 (2015) 473.
[41] B.K. Tay, T.H.T. Edwin, A. Olivier, D. Baillargeat, H. Li, Q. Zhang, C.C.R. Yap, From Bulk to Monolayer MoS_2: Evolution of Raman Scattering, Adv. Funct. Mater. 22 (2012) 1385.
[42] C. Lee, H. Yan, L.E. Brus, T.F. Heinz, J. Hone, S. Ryu, Anomalous Lattice Vibrations of Single-and Few-Layer MoS_2, ACS Nano 4 (2010) 2695.
[43] H.S.S. Ramakrishna Matte, A. Gomathi, A.K. Manna, D.J. Late, R. Datta, S.K. Pati, C.N.R. Rao MoS_2 and WS_2 Analogues of Graphene, Angew. Chem. Int. Ed. 122 (2010) 4153.
[44] D. Xie, W.J. Tang, D.H. Wang, D. Zhou, F. Shi, X.L. Wang, C.D. Gu, J.P. Tu, Integrated 3D Porous C-MoS_2/Nitrogen-Doped Graphene Electrode for High Capacity and Prolonged Stability Lithium Storage, J. Power Sources 296 (2015) 392.
[45] J.M. Jeong, K.G. Lee, S.J. Chang, J.W. Kim, Y.K. Han, S.J. Lee, B.G. Choi, Ultrathin Sandwich-Like MoS_2@N-Doped Carbon Nanosheets for Anodes of Lithium Ion Batteries, Nanoscale 7 (2015) 324.
[46] M.A. Pimenta, G. Dresselhaus, M.S. Dresselhaus, L.G. Cancado, A. Jorio, R. Saito, Studying Disorder in Graphite-Based Systems by Raman Spectroscopy, Phys. Chem. Chem. Phys. 9 (2007) 1276.

[47] M.S. Dresselhaus, G. Dresselhaus, R. Saito, A. Jorio, Raman Spectroscopy of Carbon Nanotubes, Phys. Rep. 409 (2005) 47.
[48] F. Zhou, S. Xin, H.W. Liang, L.T. Song, S.H. Yu, Carbon Nanofibers Decorated with Molybdenum Disulfide Nanosheets: Synergistic Lithium Storage and Enhanced Electrochemical Performance, Angew, Chem. Int. Ed. 126 (2014) 11736.
[49] M. Wang, G. Li, H. Xu, Y. Qian, J. Yang, Enhanced Lithium Storage Performances of Hierarchical Hollow MoS_2 Nanoparticles Assembled from Nanosheets, ACS Appl. Mater. Interfaces 5 (2013) 1003.
[50] X. Zuo, K. Chang, J. Zhao, Z. Xie, H. Tang, B. Li, Z. Chang, Bubble-Template-Assisted Synthesis of Hollow Fullerene-Like MoS_2 Nanocages as a Lithium Ion Battery Anode Material, J. Mater. Chem. A 4 (2016) 51.
[51] J. Kong, C. Zhao, Y. Wei, X. Lu, MoS_2 Nanosheets Hosted in Polydopamine-Derived Mesoporous Carbon Nanofibers as Lithium-Ion Battery Anodes: Enhanced MoS_2 Capacity Utilization and Underlying Mechanism, ACS Appl. Mater. Interfaces 7 (2015) 24279.
[52] Z. Wang, T. Chen, W. Chen, K. Chang, L. Ma, G. Huang, D. Chen, J.Y. Lee, CTAB-Assisted Synthesis of Single-Layer MoS_2-Graphene Composites as Anode Materials of Li-Ion Batteries, J. Mater. Chem. A 1 (2013) 2202.
[53] W. Qiu, J. Xia, S. He, H. Xu, H. Zhong, L. Chen, Facile Synthesis of Hollow MoS_2 Microspheres/Amorphous Carbon Composites and Their Lithium Storage Properties, Electrochim. Acta 117 (2014) 145.
[54] Z. Fan, B. Wang, Y. Xi, X. Xu, M. Li, J. Li, P. Coxon, S. Cheng, G. Gao, C. Xiao, G. Yang, K. Xi, S. Ding, R.V. Kumar, A $NiCo_2O_4$ Nanosheet-Mesoporous Carbon Composite Electrode for Enhanced Reversible Lithium Storage, Carbon 99 (2016) 633.